Check for updates

A multifunctional Co-doped BiFeO₃ nanocomposite: a promising candidate for photocatalytic degradation, antibacterial activity, and antioxidant applications†

Devender Jalandhara,[a] Sanjeev Kumar,*[b] Jasvir Dalal, [ID][c] Supreet,[d] Gautam Singh,[e] Sandeep Kumar,[f] Rahul Badru, [ID][g] Yadvinder Singh,[h] Satya Vir Sharma*[i] and Sandeep Kaushal [ID]*[i]

This study investigates the synthesis and multifunctional applications of a cobalt-doped bismuth ferrite (Co@BFO) nanocomposite, emphasizing its efficacy in photocatalytic degradation of malachite green (MG) dye, antibacterial activity against foodborne pathogens, and antioxidant capacity. The Co@BFO nanocomposite was synthesized *via* a hydrothermal method, exhibiting a crystallite size of approximately 30 nm and a surface area of 16.2 m^2 g^{-1}. Under sunlight irradiation, the nanocomposite achieved a remarkable 97% degradation of MG dye at a concentration of 15 mg L^{-1} within 120 minutes. The degradation kinetics followed a pseudo-first-order model with a rate constant of 0.0289 min^{-1}. The Co@BFO nanocomposite demonstrated significant antibacterial effects against *Klebsiella pneumoniae* and *Bacillus cereus*, achieving an MIC of 10 μg mL^{-1}. Additionally, it exhibited a DPPH radical scavenging activity ranging from 14.8% to 84.8% at concentrations between 2.5 to 15 mg L^{-1}, with an IC$_{50}$ value of 11.13 mg L^{-1}. These results confirm that the Co@BFO nanocomposite not only effectively degrades organic pollutants, but also serves as a potent antimicrobial and antioxidant agent. This multifunctionality suggests its potential for diverse applications in environmental remediation and public health.

1. Introduction

The increasing prevalence of hazardous organic pollutants and pathogenic bacteria in aquatic environments poses a significant threat to ecosystems and human health.[1–3] Since the microorganisms in wastewater have posed a serious threat to human health, it is usually imperative to eradicate the germs in order to prevent illnesses.[4] Similarly, among the different pollutants, synthetic dyes are of major concern due to their widespread use in various industries, including textiles, pharmaceuticals, and aquaculture. Malachite green (MG) dye, often referred to as triarylmethane dye, is an extremely harmful dye that is a member of the synthetic pollutant group of dyes that are used extensively in a wide range of sectors because of its affordability, efficacy, and accessibility. It has a considerable solubility in water as well as organic solvents.[5] Silk, wool, jute, leather, cotton, paper, and acrylic are among the sectors that use it for dyeing operations. When MG dye is dumped into natural water bodies, it causes irreparable damage to the aquatic cycle since it is highly toxic, persistent, mutagenic, and carcinogenic, according to studies.[6] Owing to the carcinogenic properties of MG dye, it has been documented to pollute aquatic life, that, when consumed, may trigger genotoxic problems, and adverse impacts on fertility, as well as failure of the liver, heart and kidneys.

The persistence of such a hazardous dye in the environment, coupled with its toxic and carcinogenic properties, necessitates the development of effective remediation strategies. Conventional treatment methods, such as adsorption, coagulation, and chemical oxidation, often fall short in effectively removing these contaminants, leading to an urgent need for innovative and sustainable solutions.[7–9]

[a] *Maharshi Dayanand Saraswati University, Ajmer, Rajasthan, India*

[b] *Department of Physics, Chandigarh University, Gharuan, Mohali, Punjab, India. E-mail: kumarsanju25@gmail.com*

[c] *Department of Physics, Rajdhani College, University of Delhi, Delhi, India*

[d] *Amity School of Applied Sciences, Amity University, Haryana, India*

[e] *Department of Applied Physics, Amity Institute of Applied Sciences, Amity University Uttar Pradesh, Noida, India*

[f] *Department of Chemistry, Akal University, Talwandi Sabo, Bathinda, Punjab, India*

[g] *Sri Guru Granth Sahib World University, Fatehgarh Sahib, Punjab, India*

[h] *Department of Botany, Central University of Punjab, Bathinda, Punjab, India*

[i] *Regional Institute of Education, National Council of Educational Research and Training, Ajmer, Rajasthan, India. E-mail: kaushalsandeep33@gmail.com, svsriea@yahoo.co.in*

† Electronic supplementary information (ESI) available. See DOI: https://doi.org/10.1039/d4ma01053a

Photocatalysis has emerged as a promising technology for the degradation of organic pollutants in water.[10] It utilizes solar energy to drive redox reactions, resulting in the breakdown of contaminants into less harmful substances.[11–13] Bismuth ferrite ($BiFeO_3$), a perovskite-type oxide, has gained considerable attention as a potential photocatalyst due to its favourable bandgap of approximately 2.1 eV, ferroelectric properties, and inherent stability under various environmental conditions. Though, the photocatalytic efficacy of $BiFeO_3$ is often limited by its relatively low charge separation and light absorption capabilities, particularly under visible light.[14,15]

To address these limitations, various doping approaches have been employed to improve the photocatalytic performance of $BiFeO_3$. Cobalt (Co) doping has shown promise in improving charge separation, extending light absorption into the visible range, and growing the surface area of the material.[16–19] By modifying the electronic structure and lattice parameters of $BiFeO_3$, Co doping can significantly enhance photocatalytic activity, making it a viable option for environmental remediation applications.[20–22] The incorporation of Co^{2+} ions into the $BiFeO_3$ lattice facilitates the generation of reactive oxygen species (ROS), which show a vital role in the degradation of organic pollutants.

In addition to photocatalysis, the multifunctional applications of the Co@BFO-III nanocomposite extend to its antibacterial and antioxidant properties. The cumulative resistance of pathogenic bacteria to conventional antibiotics highlights the necessity for alternative antimicrobial agents.[23–25] Metallic nanoparticles work as a non-specific bactericidal agent without binding with a specific receptor on the bacterial cell wall and are able to reduce the resistance by bacteria with enhanced antibacterial activity.[26–28] The mode of action of metal-based nanocomposites as antibacterial agents involves disturbance of the permeability of the plasma membrane by disrupting the cell wall, induction of oxidative stress, disruption of metabolic pathways and DNA damage.[29,30] The antibacterial activity of metal oxides, including Co-doped $BiFeO_3$, has been documented, showcasing their potential to combat foodborne pathogens such as *Klebsiella pneumoniae* and *Bacillus cereus*. Furthermore, the antioxidant capacity of these materials offers additional benefits in reducing oxidative stress, contributing to their multifunctionality. The antioxidant activity of metallic nanoparticles is attributed to their smaller size and ability to provide hydrogen to free radicals for the formation of non-radical compounds.[31,32]

Inspired by the discussion aforementioned, the Co-doped $BiFeO_3$ nanocomposite was fabricated employing an eco-friendly hydrothermal method. As anticipated, the fabricated Co-doped $BiFeO_3$ nanocomposite might enhance the photocatalytic, antibacterial and antioxidant activity. The fabricated Co-doped $BiFeO_3$ nanocomposite was systematically employed for the degradation of malachite green dye under the exposure of visible light. Various factors influencing the photodegradation, including the effect of concentration, pH effect, and dosage effect were performed. The radical scavenger test was then used to assess the involvement of reactive oxygen species

(ROS) to the photocatalytic activity. Additionally, the antibacterial and antioxidant activities of the as-synthesized nanocomposite have also been explored. By addressing the pressing need for effective and multifunctional materials in environmental remediation and public health, this research aims to contribute valuable insights and innovative solutions in the field of nanotechnology. The findings from this study will boost our understanding of the photocatalytic mechanisms involved in dye degradation and provide a basis for the growth of advanced nanocomposite materials for a range of applications.

2. Experimental section

2.1 Materials

The following reagents were utilized in this study: iron(III) nitrate nonahydrate ($Fe(NO_3)_3 \cdot 9H_2O$), with a molecular weight of 404.00 g mol^{-1} and a purity of $\geq 98\%$ (Sigma Aldrich); bismuth(III) nitrate pentahydrate ($Bi(NO_3)_3 \cdot 5H_2O$), with a molecular weight of 485.07 g mol^{-1} and a purity of $\geq 99.99\%$ (Sigma Aldrich); cobalt(II) nitrate hexahydrate ($Co(NO_3)_2 \cdot 6H_2O$), with a molecular weight of 291.03 g mol^{-1} and a purity of $\geq 98\%$ (American Elements); and malachite green ($C_7H_7N_2Cl$), with a molecular weight of 319.85 g mol^{-1} and a purity of $\geq 95\%$ (Sigma Aldrich). Additionally, nitric acid (HNO_3) at a concentration of 70% with a purity of $\geq 99\%$ was sourced from Loba Chemie Pvt. Ltd; polyvinyl pyrrolidone (PVP), with a molecular weight of 40 000 g mol^{-1} and a purity of $\geq 99\%$; potassium hydroxide (KOH), with a molecular weight of 56.11 g mol^{-1} and a purity of $\geq 85\%$; and sodium hydroxide (NaOH), with a molecular weight of 40.00 g mol^{-1} and a purity of $\geq 98\%$ (both from Loba Chemie Pvt. Ltd). All chemicals were utilized without further purification to maintain their intrinsic properties, and double-distilled (DD) water was employed throughout the study to ensure the elimination of contaminants that could interfere with the synthesis and characterization processes.

2.2 Fabrication of the Co@BiFeO$_3$ nanocomposite

The eco-friendly hydrothermal method was used for the synthesis of th eCo@$BiFeO_3$ nanocomposite.[33] In this standard procedure, bismuth nitrate (5×10^{-3} M) and ferric nitrate (5×10^{-3} M) were dissolved in double distilled water, then 2 mL of HNO_3 (1×10^{-3} M) was introduced gradually into the solution to obtain a clear solution. After introducing 5 mg of PVP to the aforementioned solution, the solution was subjected to an ultrasonic treatment for roughly half an hour. The precursor solution was then supplemented dropwise with 12 mL of KOH (12 M). Following another 3 hours of magnetic stirring to achieve a fully blended solution, the mixture was shifted to a Teflon autoclave and heated to 200 °C for ten hours. Thereafter, the as obtained material was cooled, washed and dried. On the other hand, for the fabrication of the Co@$BiFeO_3$ nanocomposites, to the precursor solution the desired quantity of cobalt nitrate was added. The resulting mixtures were labelled as BFO (0% Co), Co@BFO-I (3% Co), Co@BFO-II (5% Co), Co@BFO-III (10% Co), and Co@BFO-I (15% Co), respectively.

## 2.3 Physical characterization

Various instrumental approaches were used to characterize the fabricated nanocomposite's characteristics. An FTIR spectrophotometer was employed to record the FTIR spectra (Bruker Alpha-T). The crystallinity and elemental constitution were measured using the X-ray diffractometer (XRD, X'Pert PRO) and X-ray photoelectron spectroscopy (XPS, Thermo Fisher Scientific Escalab Xi+), accordingly. The morphology of the nanocomposite was investigated using an HRTEM (Jeol Jem 2100 Plus) and a FESEM-EDS (Carl Zeiss Supra 55). The Brunauer–Emmett–Teller (BET) technique was employed to investigate the adsorption properties. An ultraviolet-visible spectrometer was used to track the breakdown of the dye.

2.4 Photocatalytic experiment

MG dye, a synthetic organic dye commonly used in textile industries, was selected as the model organic contaminant to evaluate the photocatalytic performance of the synthesized nanocomposite samples. The photodegradation potential was assessed under direct sunlight exposure, simulating natural environmental conditions. The photocatalytic activity investigation was conducted in 250 mL beakers placed on magnetic stirrers to ensure uniform mixing. For each experiment, 0.02 g of the as-prepared photocatalyst (Co@BiFeO$_3$ nanocomposite) was added to 100 mL of a malachite green solution at a concentration of 10 mg L^{-1}. This initial concentration allows for clear observation of the photocatalytic activity and its kinetics. To achieve adsorption–desorption equilibrium, the solution was allowed to stand in the dark for 30 minutes. This step is crucial, as it ensures that the photocatalyst adsorbs malachite green molecules from the solution, which subsequently facilitates the photocatalytic degradation process. In addition to the photocatalytic experiments, control experiments were conducted to assess the inherent photodegradation of malachite green without the catalyst. This control involved exposing the dye solution to sunlight for the same duration without the addition of the Co@BiFeO$_3$ nanocomposite. This comparison helps establish the effectiveness of the photocatalyst in enhancing the degradation of MG.

After establishing equilibrium, the suspension was exposed to sunlight. At specified intervals, approximately 5–6 mL of the mixture was withdrawn, and the concentration of malachite green remaining in the solution was quantified using a UV-Vis spectrophotometer, measuring absorbance at the characteristic wavelength of 620 nm for MG.

The degradation of malachite green can be represented by the following reaction:

$$C_{23}H_{25}ClN_2 \text{ (aq)} + h\nu \rightarrow \text{degradation products}$$
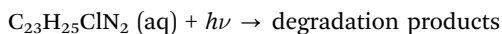
where $h\nu$ represents the photons absorbed by the photocatalyst, leading to the degradation of the dye into less harmful byproducts.

The rate of MG decomposition was calculated using the following equation:

$$\text{Decomposition effectiveness} = \frac{C_e - C_t}{C_e} \times 100$$

where C_e is the concentration of MG dye at equilibrium (after the dark adsorption period) and C_t is the concentration at time t during sunlight exposure.

Furthermore, the photocatalytic performance was examined under varying pH conditions to understand the effect of acidity or alkalinity on the degradation mechanism. The effect of different catalyst dosages (ranging from 10 to 25 mg) on the degradation rate was also assessed to optimize the photocatalyst loading.

2.5 In vitro biomedical applications

2.5.1 Antibacterial properties. The antibacterial potential of the synthesized nanoparticles against foodborne pathogens, specifically *Klebsiella pneumoniae* (Gram-negative) and *Bacillus cereus* (Gram-positive), was evaluated using the agar well diffusion assay.[34] This study seeks to advance the current understanding in the field of nanomedicine by elucidating the efficacy of these nanoparticles as antimicrobial agents. To assess antibacterial activity, approximately 25 to 30 mL of cooled nutrient agar (Hi Media) was poured into sterilized Petri dishes and incubated overnight at 37 °C in a BOD incubator to ensure the absence of contamination. The bacterial strains were initially cultured in Nutrient Broth (Hi Media) for 24 hours, with culture vials maintained at 37 °C under agitation at 150 rpm to achieve optimal growth conditions. After incubation, the bacterial cultures were diluted to a cell density of 10^{-6} CFU mL^{-1}, ensuring consistent inoculation across all test plates. The suspension was evenly spread onto the surface of individual agar plates using a sterile glass spreader and allowed to rest for 2 hours under controlled conditions to facilitate attachment. Wells measuring 6 mm in diameter were then created in the agar using a sterilized stainless-steel borer. Each well was filled with 20 µL of the nanocomposite sample. The loaded plates were incubated for 18 hours at 37 °C in the BOD incubator. The antibacterial activity was assessed by measuring the diameter of the inhibition zones surrounding each well in millimeters, providing a quantitative measure of the antibacterial efficacy of the nanocomposite. This method allowed for direct observation of the interaction between the nanocomposite and bacterial growth, reinforcing the significance of this research in addressing foodborne pathogens. Additionally, to determine the minimum inhibitory concentration (MIC), the effects of various concentrations of the synthesized Co@BFO nanocomposite on the growth of both *K. pneumoniae* and *B. cereus* were investigated, following established methodologies.[35] The results of this investigation will provide crucial data regarding the threshold concentrations needed to inhibit bacterial growth effectively.

2.5.2 Antioxidant property. DPPH radical scavenging assay: the DPPH (2,2-diphenyl-1-picrylhydrazyl) free radical scavenging assay was conducted according to the methodology established by Peddi *et al.*,[36] aiming to quantitatively assess the antioxidant activity of the synthesized Co@BFO nanocomposite. A series of concentrations of the synthetic Co@BFO nanocomposite were prepared in methanol, ranging from 0.1 mg mL^{-1} to 1.0 mg mL^{-1}, to systematically investigate their

efficacy in scavenging DPPH free radicals. For the assay, a freshly prepared 0.135 mM DPPH methanol solution was accurately measured and combined with 1 mL of each concentration of Co@BFO nanocomposite to form the reaction mixture. The DPPH solution, known for its deep violet color, serves as a stable free radical that undergoes reduction in the presence of antioxidants. The mixture was incubated in the dark at room temperature for 30 minutes to minimize photodegradation of the DPPH radical, allowing optimal interaction between the nanocomposite and the radical species. The reduction in DPPH concentration was quantified by measuring the absorbance at 517 nm using a UV-Vis spectrophotometer, a standard method for determining the antioxidant capacity. The degree of discoloration, which corresponds to the scavenging ability of the nanocomposites, was assessed against a blank control containing only DPPH and methanol. All experiments were performed in triplicate to ensure reproducibility and statistical validity, with L-ascorbic acid employed as a standard antioxidant for comparative analysis and methanol as the reference blank.

The radical scavenging activity of the synthesized Co@BFO nanocomposites was calculated using the following formula:

$$\text{DPPH scavenging activity (\%)} = \frac{A_{control} - A_{sample}}{A_{control}} \times 100$$

This quantitative assessment allows for a precise determination of the radical scavenging capacity of the nanoparticles, providing important implications for their potential applications in alleviating oxidative stress.

2.5.2.1 Total antioxidant capacity. The total antioxidant capacity (TAC) of the biosynthesized CuO nanoparticles at various concentrations was determined using the phosphomolybdenum method,[37] a widely recognized assay for quantifying antioxidant activity. This method is based on the reduction of Mo(VI) to Mo(V) in acidic medium, resulting in the formation of a green phosphomolybdic complex that can be spectrophotometrically analysed. In this assay, 400 μL of the Co@BiFeO$_3$ nanocomposite sample was combined with 3.6 mL of the phosphomolybdenum reagent, which consists of ammonium molybdate dissolved in sulfuric acid. The reaction cocktail was mixed thoroughly to ensure complete interaction between the nanoparticles and the reagent. The mixtures were then incubated at 95 °C for one hour and 30 minutes to facilitate the reduction of Mo(VI) ions by the antioxidants present in the Co@BiFeO$_3$ nanocomposite, leading to the formation of the characteristic green phosphomolybdic complex. The antioxidant capacity of each concentration of Co@BiFeO$_3$ nanocomposite was then calculated as a percentage relative to the control, using ascorbic acid as a standard reference for comparison.

3. Results and discussion

3.1 UV-Visible analysis

The UV-visible absorption spectra of the BiFeO$_3$ and Co@BFO nanocomposites were analyzed to investigate the effect of cobalt doping on the optical properties and absorption characteristics. As shown in Fig. S1a (ESI†), the undoped BFO sample exhibits an absorption edge at 535.2 nm, marking the onset of light absorption in the visible range. The red shift in the absorption edge observed with increasing cobalt doping suggests a narrowing of the band gap, which allows for the absorption of longer wavelengths of light. For the Co@BFO-I, sample, the absorption edge shifts to 545.7 nm, the Co@BFO-II sample displays an absorption edge at 554.1 nm, the Co@BFO-III sample shows an absorption edge at 565.3 nm, and the Co@BFO-IV sample exhibits the largest red shift at 573.1 nm. The red shift in the absorption edge with increasing cobalt concentration is consistent with the reduction in band gap, which is influenced by the introduction of additional energy states within the material's electronic structure due to Co doping.

The Tauc plot shown in Fig. S1b (ESI†) is used to determine the precise optical band gap of each sample. The band gap values calculated from the Tauc plot are 2.12 eV for BFO, 2.04 eV for Co@BFO-I, 1.97 eV for Co@BFO-II, 1.91 eV for Co@BFO-III, and 1.81 eV for Co@BFO-IV. These values confirm the trend of a decreasing band gap with increasing cobalt doping, which is consistent with the red shift in the absorption edge observed in the UV-visible spectra.

3.2 XRD analysis

The X-ray diffraction (XRD) analysis was performed to examine the crystallinity and phase composition of the synthesized Co@BiFeO$_3$ (Co@BFO) nanocomposites, as depicted in Fig. 1. The XRD patterns reveal distinct diffraction peaks corresponding to the rhombohedral crystal structure of bismuth ferrite (BFO), aligning with JCPDS card no. 01-186-1518. The characteristic peaks observed at approximately 22.3°, 32.5°, 35.5°, 40.5°, 48.3°, and 57.3° correspond to the (012), (104), (110), (113), (202), and (211) planes, respectively.[38] The sharp and intense peaks indicate a high degree of crystallinity, which
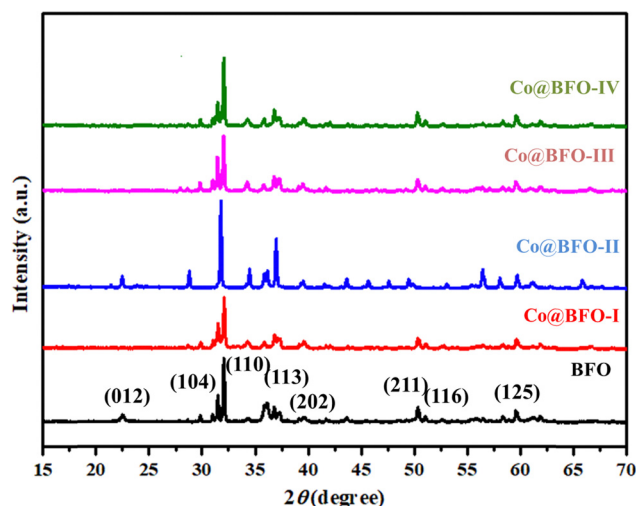

Fig. 1 XRD patterns of the as-prepared BFO and Co@BFO nanocomposites.

is crucial for photocatalytic applications, as it facilitates efficient charge transport and minimizes electron–hole recombination.

In the XRD pattern of bare $BiFeO_3$, the prominent peaks signify that the material retains its perovskite structure, essential for photocatalytic efficiency. The lattice constants were calculated to be $a = b = 5.57$ Å and $c = 13.86$ Å, corresponding to the space group $R3c$ (no. 161).[39] This structural stability is critical for photocatalytic applications, as it supports the functionality and longevity of the material under reaction conditions. The introduction of Co^{2+} ions results in a notable shift in the (110) peak from $32.5°$ for the BFO sample to approximately $32.2°$ for Co@BFO-I. This shift indicates the incorporation of Co^{2+} ions into the BFO lattice, likely substituting Bi^{3+} or Fe^{3+} ions. The smaller ionic radius of Co^{2+} (0.69 Å) compared to Bi^{3+} (1.11 Å) allows for this substitution without significant distortion of the crystal lattice.[40,41] The enhancement in peak intensity further suggests that the doping concentration is within an optimal range, promoting crystallinity. For Co@BFO-II, the XRD pattern shows a similar trend, with the (110) peak shifting to $31.9°$ and an increase in the overall intensity of the diffraction peaks. This suggests that the structural integration of Co^{2+} ions is enhancing the crystallinity of the nanocomposite. The solid-state reaction can be described by the following substitution reaction:

$$Bi^{3+} + Co^{2+} \rightarrow Co^{2+} + BFO$$
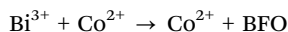
The successful incorporation of cobalt ions is further supported by the maintenance of distinct BFO peaks, indicating that the core structure remains intact while benefiting from the properties imparted by cobalt doping.

The Co@BFO-III sample exhibits a marked increase in peak intensity and a further shift in the (110) peak to $31.7°$, suggesting optimal cobalt incorporation. The improved crystallinity and structural stability at this doping level can be attributed to the effective balance between Bi^{3+} and Co^{2+} ions, which enhances the photocatalytic properties by facilitating charge separation. Studies have shown that such optimally doped materials exhibit better photocatalytic performance due to minimized recombination of charge carriers, which is essential for effective catalytic activity. However, in the XRD pattern for Co@BFO-IV, a slight broadening of the peaks is observed, indicating the onset of strain or possible phase segregation due to excessive cobalt incorporation. The (110) peak shifts further to approximately $31.5°$, but the broadening suggests that the material may be approaching a critical threshold of cobalt concentration that leads to structural instability. This observation aligns with the literature indicating that while doping can enhance photocatalytic properties, excessive doping may result in increased defects and reduced crystallinity, negatively impacting photocatalytic efficiency.

The crystallite sizes, calculated using Scherrer's equation, ranged from 30.23 nm for Co@BFO-IV to 39.71 nm for Co@BFO-I. Notably, Co@BFO-III, with a size of 32.11 nm, exhibited the most favourable characteristics for photocatalytic activity, suggesting an optimal balance between crystallinity and size that may enhance photocatalytic performance.

Therefore, based on its optimal crystallinity and size, Co@BFO-III was selected for further characterization using field emission scanning electron microscopy (FESEM).

3.3 FESEM analysis

The morphological characteristics of the synthesized $BiFeO_3$ (BFO) and Co-doped $BiFeO_3$ (Co@BFO) nanocomposites were analysed using FESEM. The FESEM images of the Co@BFO-III nanocomposite are displayed in Fig. 2. As revealed, from the images that nanocomposite exhibited a pallet-like structure, and each pallet has a width of approximately 40 nm. The FESEM images of all other as-prepared samples are shown in the ESI† (Fig. S2 and S3).

To gain a comprehensive understanding of the elemental composition of the Co@BFO-III nanocomposite, energy dispersive X-ray spectroscopy (EDX) was employed, as illustrated in Fig. 3. The EDX spectrum clearly indicates the presence of key elements: bismuth (Bi), iron (Fe), cobalt (Co), and oxygen (O). The characteristic peaks corresponding to the K and L lines of these elements confirm the successful incorporation of cobalt into the $BiFeO_3$ lattice, essential for enhancing photocatalytic activity. The accompanying elemental mapping further clarifies the distribution of these elements across the nanocomposite. Each element is depicted in distinct colours to facilitate differentiation, with brighter areas on the elemental maps indicating regions with higher concentrations of specific elements. The maps confirm the homogeneous distribution of Bi, Fe, Co, and O throughout the Co@BFO-III nanocomposite, which is critical for ensuring uniform photocatalytic performance. Such uniformity indicates that cobalt doping is effectively integrated into the crystal structure without segregation, which could otherwise lead to reduced catalytic efficiency.

The EDS data reinforce the XRD findings, supporting the hypothesis that the structural modifications due to cobalt incorporation are uniform and consistent across the sample. The elemental analysis also provides insights into the stoichiometry of the nanocomposite, which is vital for understanding its reactivity and performance in photocatalytic applications. The consistent distribution of elements observed in the elemental mapping suggests that the Co@BFO-III nanocomposite is well-prepared for photocatalytic applications, enhancing the likelihood of effective charge transfer and overall catalytic efficiency. These findings highlight the importance of thorough
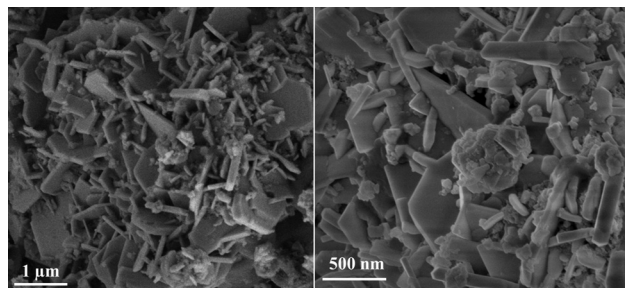

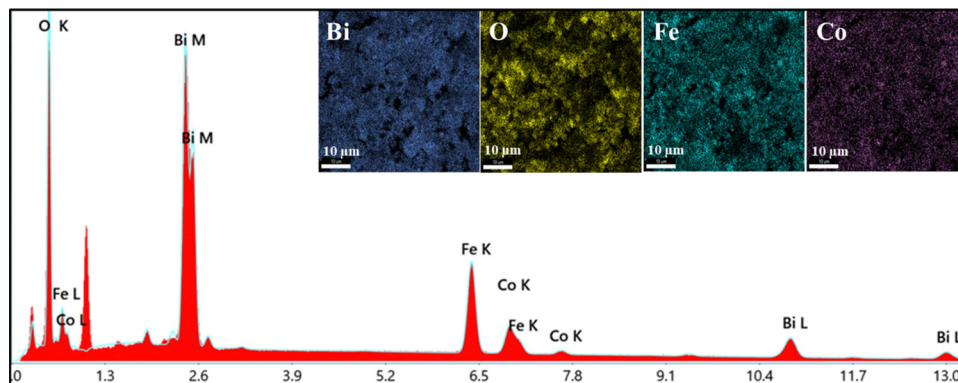Fig. 2 FESEM micrographs of the Co@BFO-III nanocomposite.

Fig. 3 EDS spectra and mapping of the Co@BFO-III nanocomposite.

compositional analysis in validating the synthesis process and optimizing the performance of photocatalytic materials.

3.4 HRTEM analysis

The high-resolution transmission electron microscopy (HRTEM) analysis of the Co@BFO-III nanocomposite, illustrated in Fig. 4, provides critical understandings of the nanoscale structural features and crystallinity of the material. Images (a) and (b) show that the microstructure of the synthesized nanocomposite is remarkably homogeneous, characterized by well-dispersed plate-like particles. The uniform distribution and size of the nano-particles are essential, as they contribute to maximizing the surface area available for photocatalytic reactions, thereby enhancing reactivity. In image (c), the HRTEM images reveal distinct lattice fringes with measured interplanar spacings of 0.39 nm and 0.27 nm, corresponding to the (012) and (110) crystal planes of the rhombohedral $BiFeO_3$ structure, respectively. The clear

visibility of these lattice fringes signifies the high crystallinity of the Co@BFO-III nanocomposite, which is crucial for facilitating efficient charge transport during photocatalytic processes. The well-defined lattice fringes indicate that the incorporation of Co^{2+} ions into the $BiFeO_3$ lattice has been successful without introducing significant disorder, thus preserving the structural integrity necessary for optimal photocatalytic performance. Furthermore, a histogram depicting the particle size distribution of the Co@BFO-III nanocomposite as obtained from TEM analysis has been displayed in Fig. S4 (ESI†).

Furthermore, the selected area electron diffraction (SAED) pattern shown in panel (d) provides additional confirmation of the crystalline phase of the Co@BFO-III nanocomposite. The diffraction spots correspond to various crystallographic orientations, specifically the (202), (024), (300), (018), and (012) planes, demonstrating a significant degree of crystalline order. This degree of crystallinity is indicative of the material's potential for efficient photocatalytic activity, as higher crystallinity is often associated with improved charge separation and reduced electron–hole recombination. The observed microstructural features, including the uniform plate-like morphology and distinct lattice parameters, suggest that Co@BFO-III is well-suited for photocatalytic applications.

3.5 FTIR analysis

To explore the functional groups and chemical bonding characteristics of the as-synthesized photocatalysts, Fourier transform infrared (FTIR) spectroscopy was employed, as illustrated in Fig. 5. The FTIR spectra exhibit several characteristic vibrational absorption bands across all synthesized materials, indicating the presence of various functional groups and chemical interactions. Notably, a significant absorption band appears at 1384 cm^{-1}, which is attributed to C–C stretching vibrations, while bands at 1601 cm^{-1} and 2917 cm^{-1} correspond to C=O and C=C vibrations, respectively. These bands suggest the presence of organic contaminants or surface-adsorbed species, which could play a role in the photocatalytic processes. Moreover, the bands observed at 877 cm^{-1} and 1437 cm^{-1} indicate the presence of nitrate ions, which can influence the electronic properties of the nanocomposites and may contribute to their photocatalytic efficiency.[42] The presence of these nitrate groups
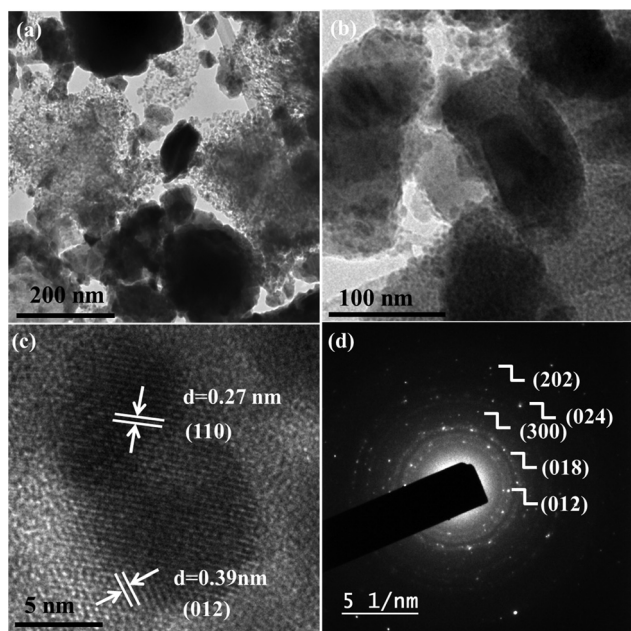

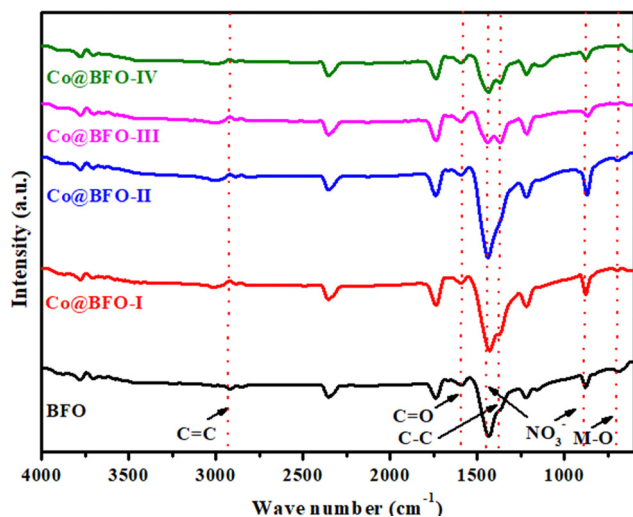**Fig. 4** (a–c) HRTEM images and (d) SAED pattern of the Co@BFO-III nanocomposite.

Fig. 5 FTIR spectra of the as-prepared BFO and Co@BFO nanocomposites.

is consistent with the synthesis route involving bismuth and cobalt nitrates, confirming successful incorporation into the final structure. Another significant band at 697 cm^{-1} is attributed to the formation of metal–oxide bonds, specifically associated with the Bi–O and Fe–O stretching vibrations in the perovskite structure of BiFeO$_3$. This metal–oxide feature is crucial for photocatalytic activity, as it signifies the presence of active sites for charge transfer processes. Interestingly, the FTIR spectra reveal slight shifts in band positions as the doping concentration increases, particularly in Co@BFO-I through Co@BFO-IV. These shifts may indicate alterations in bond strength and lengths due to cobalt doping, potentially leading to the formation of oxygen vacancies within the samples. Such vacancies are known to enhance photocatalytic activity by facilitating charge carrier separation and reducing recombination rates. In summary, the FTIR analysis confirms the successful incorporation of functional groups and the formation of metal–oxide structures within the Co@BFO nanocomposites.

3.6 XPS analysis

To explain the chemical states of the constituent elements in the Co@BFO-III nanocomposite, X-ray photoelectron spectroscopy (XPS) was conducted, as shown in Fig. 6. The survey spectrum indicates the presence of significant peaks corresponding to bismuth (Bi), iron (Fe), cobalt (Co), oxygen (O), and carbon (C) at binding energies of 158.5 eV, 711.27 eV, 780.12 eV, 530.96 eV, and 283.75 eV, respectively. The XPS spectrum of the Bi 4f region reveals two distinct peaks at 158.5 eV and 164.2 eV, which correspond to the Bi 4f$_{7/2}$ and Bi 4f$_{5/2}$ states, respectively.[43] These values confirm the presence of Bi in the +3 oxidation state, indicating successful incorporation into the Co@BFO-III nanocomposite. In the Fe 2p spectrum, the binding energies of Fe are noted at 709.7 eV and 711.8 eV, corresponding to Fe^{2+} 2p$_{3/2}$ and Fe^{3+} 2p$_{3/2}$, respectively, while a peak at 724.1 eV is assigned to Fe^{2+} 2p$_{1/2}$.[44,45] The relative peak intensities suggest a predominance of Fe^{3+} ions in the

nanocomposite, which is crucial for maintaining electronic balance and enhancing photocatalytic activity. The presence of both oxidation states indicates the potential for redox reactions during photocatalytic processes, where Fe^{3+} can facilitate electron transfer, thus improving the overall efficiency of pollutant degradation. The Co 2p spectrum displays characteristic peaks at 782.6 eV and 795.8 eV, corresponding to Co^{3+} 2p$_{3/2}$ and Co^{2+} 2p$_{1/2}$, respectively.[46] The coexistence of Co^{2+} and Co^{3+} ions is significant, as it can promote charge separation during photocatalytic reactions. The presence of Co^{3+} is particularly important because it can act as an electron acceptor, thus reducing the recombination rates of charge carriers generated during the photocatalytic process. The O 1s spectrum shows three primary peaks at 528.9 eV, 530.7 eV, and 532.6 eV, attributed to metal–oxygen (M–O) bonds, dangling bonds, and surface-adsorbed oxygen, respectively.[47] The consistent presence of surface-adsorbed oxygen may enhance the reactivity of the nanocomposite by providing additional reactive sites for photocatalytic reactions. The C 1s spectrum is deconvoluted into three peaks at 284.0 eV, 285.4 eV, and 288.5 eV, corresponding to C–C/C=C, C–O, and O–C=O configurations, respectively. The presence of these carbon species may indicate organic residues from the synthesis process or surface functionalization that can influence the photocatalytic properties of the material. In summary, the XPS analysis of Co@BFO-III provides comprehensive insights into the oxidation states and chemical environments of the constituent elements. The successful incorporation of Bi, Fe, Co, and O in their respective oxidation states underscores the potential of this nanocomposite for photocatalytic applications.

3.7 BET analysis

The N$_2$ adsorption–desorption isotherm of the Co@BFO-III nanocomposite, depicted in Fig. 7, was analyzed using the BET (Brunauer–Emmett–Teller) method to evaluate its surface area and porous characteristics. The adsorption isotherm is classified as a type IV isotherm, indicating the presence of mesopores in the nanocomposite structure. This type of isotherm is typically associated with materials exhibiting capillary condensation in mesopores, confirming that the synthesized Co@BFO-III nanocomposite possesses a porous framework suitable for adsorption applications. From the analysis, the Co@BFO-III nanocomposite is estimated to have a surface area of 16.2 m^2 g^{-1}, which, while relatively modest, is advantageous for photocatalytic activity, as it provides sufficient active sites for the adsorption of organic pollutants. The total pore volume was determined to be 0.0299 cm^3 g^{-1}, and the mean pore diameter was calculated to be 3.8 nm. This pore size falls within the mesoporous range, which is beneficial for facilitating the mass transport of reactants to the active sites during photocatalytic reactions. The combination of a suitable surface area and optimal pore size enhances the efficiency of surface-based activities, such as photocatalysis. The presence of mesopores allows for the effective diffusion of reactants and provides a larger area for interactions with the catalyst, which is crucial for improving the reaction kinetics in practical
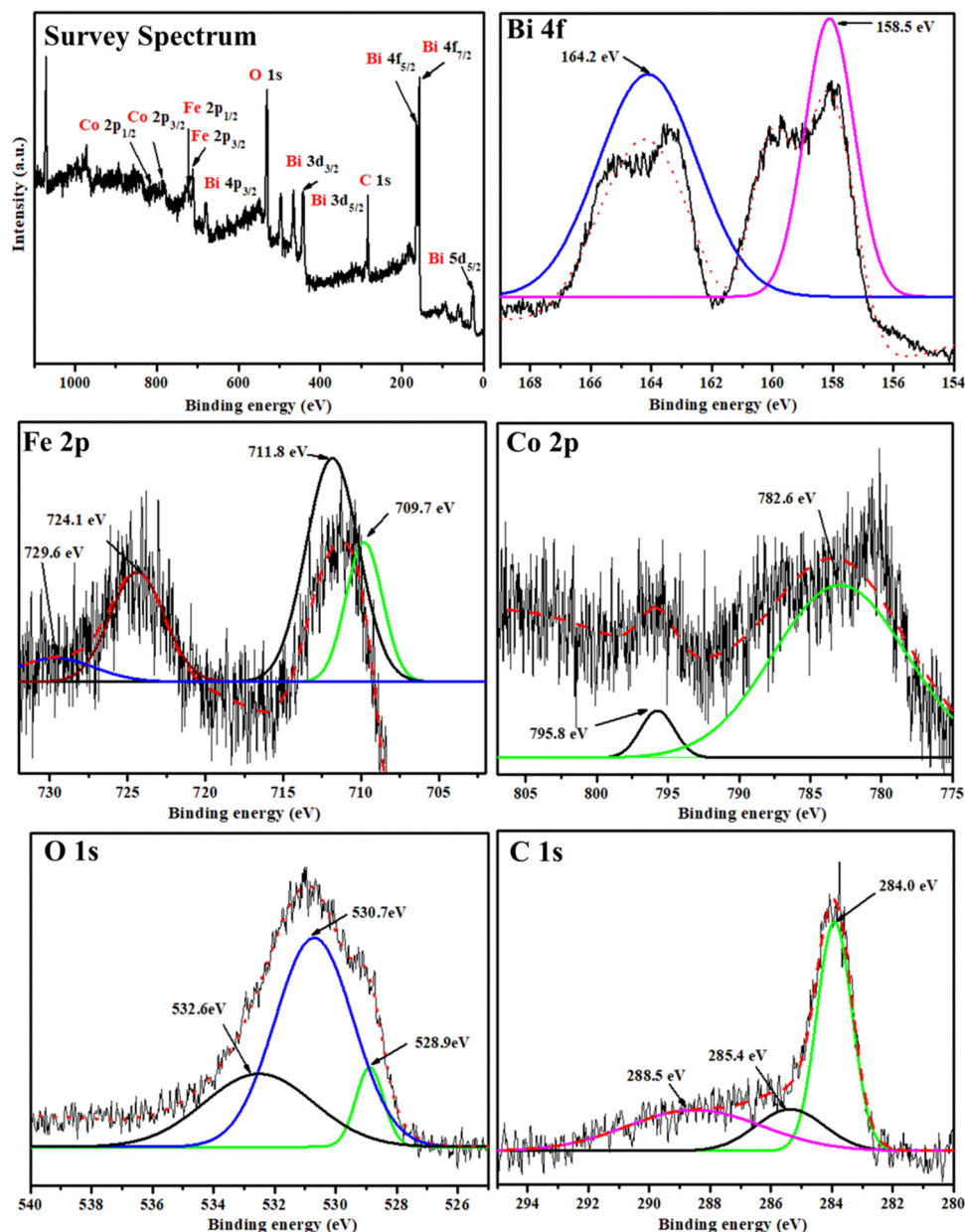
Fig. 6   XPS analysis of the Co@BFO-III nanocomposite.

applications. Overall, the N_2 adsorption–desorption results confirm that the Co@BFO-III nanocomposite has a favourable porous structure, contributing to its potential effectiveness in environmental remediation processes, particularly in the degradation of organic pollutants. Additional results for BFO, Co@BFO-I, Co@BFO-II, and Co@BFO-IV are provided in the ESI† (Fig. S5 and Table S1).

3.8   Zeta potential analysis

Zeta potential tests have been used to assess the Co@BFO-III nanocomposite's surface charge characteristics (Fig. S6, ESI†). In neutral circumstances, the nanocomposite's zeta potential was found to be −11.9 mV. Interestingly, at pH levels of 10.0 and 12.0, each, the zeta potential values appeared to be −28.0

and −31.1 mV. At a pH level of 5.0 and 3.0, on the other hand, it was found to be 10.1 and 32.9 mV, accordingly. The change in surface hydroxylation property is responsible for the variance in the Co@BFO-III nanocomposite surface charge features. The Zeta potential decreased when the hydroxylated surface was de-protonated in an alkaline environment, and increased when the hydroxylated surface was protonated in acidic conditions.

4. Photodegradation analysis

4.1   Photocatalytic performances

The photocatalytic activity of the synthesized Co@BFO-III nanocomposite was rigorously assessed through the degradation of the toxic MG dye under sunlight irradiation. The UV-
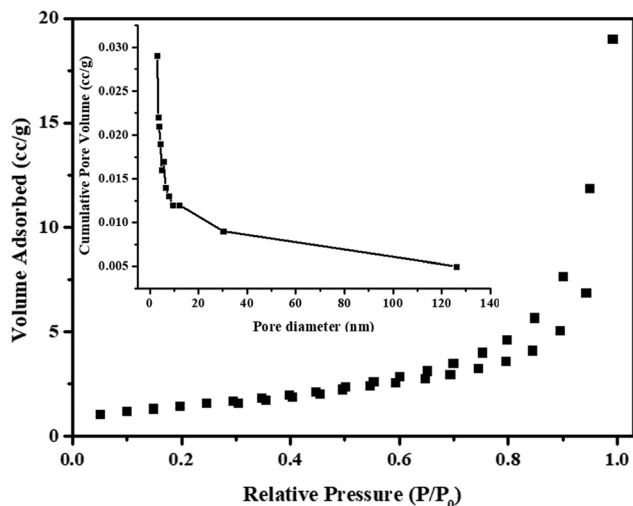
Fig. 7 N$_2$ adsorption–desorption spectra of the Co@BFO-III nanocomposite.

visible absorbance spectra, presented in Fig. 8(a), illustrate the significant changes in the absorption characteristics of MG dye over a period of 120 minutes, focusing particularly on the peak at 617 nm, which corresponds to the maximum absorbance of MG. At the initiation of the experiment, the absorbance spectrum of MG dye displayed a pronounced peak at 617 nm, indicating a high concentration of the dye in the solution. As the irradiation time increased, a progressive decrease in the intensity of this peak was observed, indicating the effective degradation of the dye molecules. This reduction in absorbance confirms the photocatalytic activity of the Co@BFO-III nanocomposite, as the dye molecules are broken down into less harmful byproducts. The observed degradation can be attributed to the enhanced photocatalytic properties of Co@BFO-III, which promotes the generation of reactive oxygen species (ROS) under sunlight exposure. The incorporation of Co^{2+} ions into the BiFeO$_3$ lattice is known to improve charge carrier dynamics by facilitating charge separation, thus increasing

the availability of hydroxyl radicals and superoxide anions that contribute to the degradation of organic pollutants.

The photocatalytic degradation of MG dye was systematically studied at different initial concentrations (5, 10, 12, and 15 mg L^{-1}) over a 120-minute period under direct sunlight irradiation. The results, as depicted in Fig. 8(b), demonstrate a clear trend: as the initial concentration of the dye increases, the percentage degradation decreases significantly. At an initial concentration of 15 mg L^{-1}, the Co@BFO-III nanocomposite exhibited the highest degradation efficiency, achieving approximately 93% removal of the MG dye after 120 minutes. This high level of degradation can be attributed to the photocatalyst's effective ability to generate reactive oxygen species (ROS), which play a crucial role in breaking down organic pollutants.[48] However, the observed decrease in degradation efficiency with increasing dye concentration can be explained by the phenomenon of light absorption and scattering within the solution. As the concentration of MG dye increases, the solution becomes opaquer, leading to higher absorption of incident light. This reduced light penetration limits the availability of photons for the photocatalytic process, as less light reaches the surface of the photocatalyst.[49] Consequently, the generation of charge carriers and reactive radicals is diminished, leading to a reduced rate of photodegradation. Moreover, the increased concentration of dye also contributes to a higher likelihood of dye–dye interactions, which may further hinder the photocatalytic activity by competing with the photocatalyst for available active sites.[50] Therefore, while higher dye concentrations result in greater total mass of the pollutant, they also create unfavourable conditions for effective degradation. In the current investigation, the optimal concentration for degradation efficiency was identified as 15 mg L^{-1} of MG dye. This concentration was selected for further studies to explore the effects of pH, catalyst dosage, and scavengers on the photocatalytic performance of the Co@BFO-III nanocomposite.

The degradation kinetics of MG dye in the presence of various photocatalysts was systematically analyzed, with the normalized concentration C_t/C_0 plotted against exposure time,
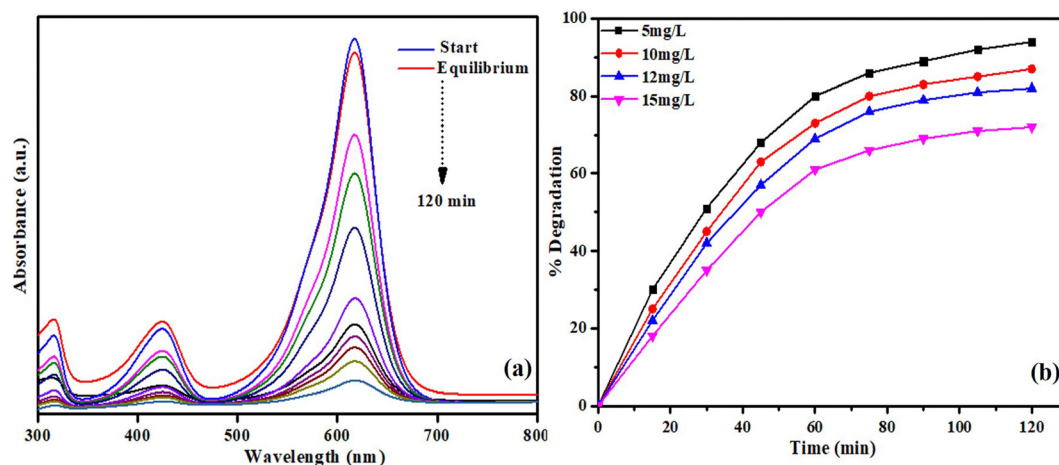

Fig. 8 (a) UV-Visible absorbance spectrum of MG dye degradation *vs.* time and (b) percentage degradation of MG dye at different initial concentrations (5, 10, 12, and 15 mg L^{-1}) over 120 minutes.
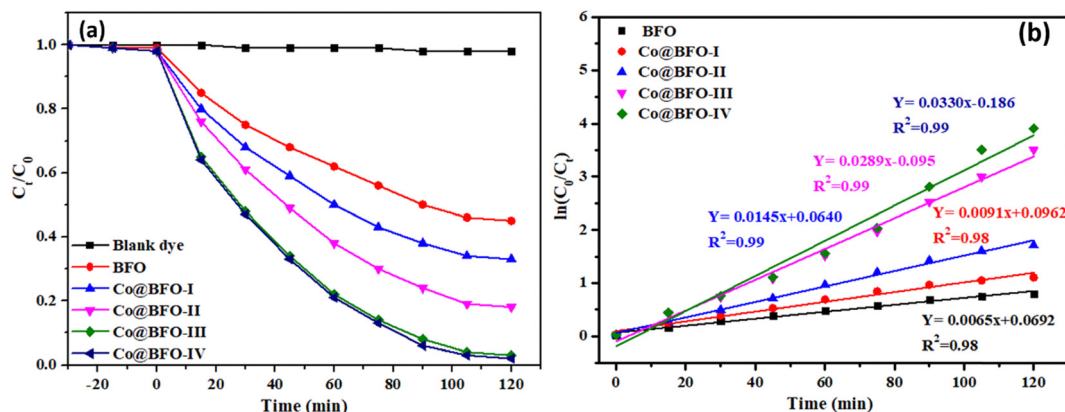
Fig. 9 (a) Degradation kinetics of MG dye *vs.* irradiation time and (b) degradation rate constants of the MG dye.

as shown in Fig. 9(a). Here, C_0 represents the initial concentration of the dye, while C_t denotes the concentration at time t. The data clearly indicate that in the absence of photocatalysts (represented by the blank dye line), the concentration of MG dye remains relatively constant, demonstrating that degradation does not occur spontaneously. This observation suggests that the presence of a photocatalyst is essential for facilitating the degradation process. Furthermore, the minimal degradation observed without light exposure reinforces the notion that photocatalytic activity is significantly enhanced under irradiation. The results underscore the critical role of light in promoting the photocatalytic reactions necessary for effective dye degradation. In stark contrast, the presence of photocatalysts leads to a marked decrease in MG dye concentration over time, particularly with Co@BFO-III, which exhibits the most significant degradation efficiency. The decline in concentration with extended irradiation time can be attributed to the effective separation of charge carriers (electrons and holes) generated in the photocatalyst upon light excitation. This charge separation is crucial for initiating oxidation–reduction reactions on the surface of the photocatalyst, which facilitates the breakdown of dye molecules into less harmful products. Quantitatively, the photocatalytic degradation efficiency varies among the different Co@BFO nanocomposites, indicating that the composition and structural properties of the catalysts directly influence their photocatalytic performance. The data suggest a correlation between the degree of cobalt doping and the photocatalytic efficiency, with optimal performance achieved at the Co@BFO-III composition.

The photocatalytic degradation efficiency of MG dye under sunlight irradiation was evaluated for various catalysts, as illustrated in Fig. 9(b). The BFO metal oxide exhibited a degradation efficiency of 56% after 120 minutes of exposure. In contrast, the Co@BFO nanocomposites demonstrated significantly enhanced photocatalytic performance, with degradation efficiencies of approximately 72% for Co@BFO-I, 86% for Co@BFO-II, and 97% for Co@BFO-III. Notably, Co@BFO-IV achieved an impressive 97.5% degradation of MG dye under the same experimental conditions. The increased photocatalytic efficiency observed with the Co@BFO nanocomposites can

be attributed to the synergistic effects of cobalt doping and the resultant enhancements in charge separation and solar light absorption.[51] The incorporation of Co^{2+} ions into the $BiFeO_3$ lattice facilitates improved electron mobility and enhances the generation of reactive oxygen species (ROS), which are crucial for effective dye degradation. Among all the prepared nanocomposites, Co@BFO-III exhibited the highest degradation efficiency, highlighting its optimal doping level. Conversely, further cobalt loading in Co@BFO-IV did not yield a significant increase in MG dye degradation, suggesting that excessive Co may adversely affect photocatalytic efficiency due to potential agglomeration or electronic structural changes that hinder charge carrier dynamics. The graphical representation of $\ln(C_0/C_t)$ *versus* time for each photocatalyst, shown in Fig. 10, indicates that the degradation of MG dye follows pseudo-first-order reaction kinetics. The linear relationship observed across all samples suggests a consistent degradation mechanism governed by the availability of active sites on the photocatalyst surface. The rate constants (k) for MG dye degradation were calculated based on the slopes of the linear plots. The values obtained for each photocatalyst are as follows: $k = 0.0065$ min^{-1} for BFO, 0.0091 min^{-1} for Co@BFO-I, 0.0145 min^{-1} for Co@BFO-II, 0.0289 min^{-1} for Co@BFO-III, and 0.0330 min^{-1} for Co@BFO-IV. The increase in k values from BFO to Co@BFO-III underscores the enhanced photocatalytic activity attributed to optimal cobalt doping. The relatively stable k value from Co@BFO-III to Co@BFO-IV further supports the conclusion that Co@BFO-III represents an optimal balance of structural and electronic properties for effective photocatalytic degradation of organic pollutants.

Effect of pH and scavengers on photocatalytic degradation of mg dye: the degradation efficiency of MG dye using the Co@BFO-III photocatalyst was evaluated under varying pH conditions and in the presence of different scavengers. Fig. 10(a) illustrates the impact of pH on the degradation efficiency, revealing that degradation improves significantly as the pH increases from acidic to neutral conditions, peaking at pH 7. The highest degradation observed at this neutral pH indicates that the surface properties of the photocatalyst are optimized, allowing for effective adsorption and interaction
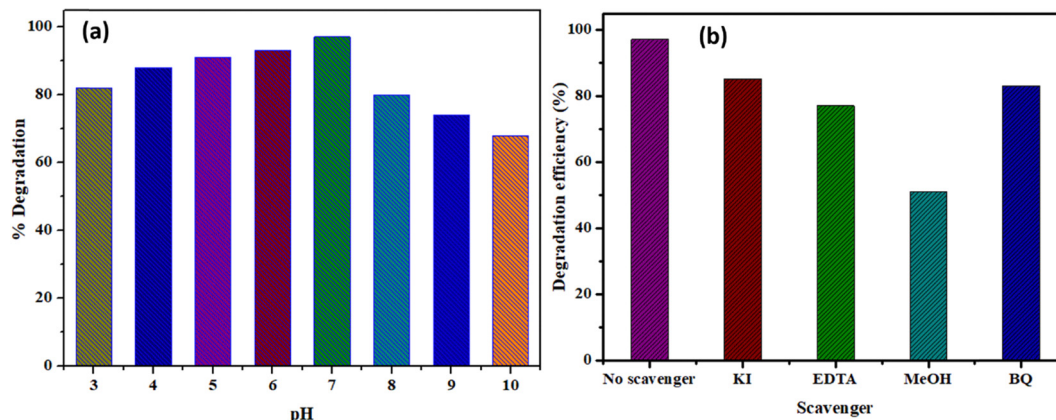
Fig. 10 (a) Effect of pH value of the solution on MG dye degradation, and (b) effect of scavengers on the degradation efficiency of MG dye over the Co@BFO nanocomposite.

between the dye molecules and reactive species generated during the photocatalytic process. In alkaline conditions, the generation of hydroxyl radicals ($^{\bullet}$OH) contributes to dye decolorization; however, the degradation efficiency decreases, potentially due to the reaction of $^{\bullet}$OH with positively charged ions, which inhibits the degradation of MG dye.[52,53]

4.2 Proposed mechanism of photocatalysis

Enhancing the degradation efficiency is mostly dependent on the fabricated nanocomposite's internal electric field and appropriate band edge potential. For photocatalytic uses, the conduction band (CB) and valence band (VB) edge potentials of heterostructures are often closely related to the reaction rate. According to our earlier research, the position of the VB and CB has been determined by the following equation:[54]

$$E_{CB} = \chi - E^{\circ} - \frac{1}{2}E_g$$

$$E_{VB} = E_{CB} + E_g$$

where χ and E_g signify the electronegativity and band gap of the nanocomposite. E° denotes the energy of free electrons on the hydrogen scale (~ 4.50 eV $vs.$ NHE). The electronegativity of the Co@BiFeO$_3$ nanocomposite has been determined to be 5.83 eV. The CB and VB band edge potentials of the Co@BiFeO$_3$ nanocomposite were determined using the equation above, and they are 0.375 and 2.28 eV, respectively, $vs.$ NHE.

The photocatalytic process is driven by various reactive species, including superoxide anions ($^{\bullet}$O$_2^-$), hydroxyl radicals ($^{\bullet}$OH), holes (h$^+$), and electrons (e$^-$). Each of these species can participate in the degradation of dye molecules; thus, identifying their roles is crucial for understanding the photocatalytic mechanism. To discern the contribution of specific reactive species, different scavengers were employed: EDTA (for h$^+$), KI (for e$^-$), MeOH (for $^{\bullet}$OH), and BQ (for $^{\bullet}$O$_2^-$). The experimental conditions remained consistent with standard photocatalytic studies to ensure comparability. As depicted in Fig. 10(b), the introduction of MeOH significantly reduced the degradation

efficiency of MG dye, indicating that $^{\bullet}$OH radicals play a critical role in the degradation process. This finding suggests that hydroxyl radicals are the primary reactive intermediates responsible for breaking down the dye molecules. In contrast, the addition of EDTA, KI, and BQ resulted in only minor reductions in photocatalytic activity, signifying that h$^+$, e$^-$, and $^{\bullet}$O$_2^-$ contribute to the degradation process but do not dominate, highlighting a synergistic effect among the reactive species. Furthermore, the degradation efficiency of MG dye is influenced by both the pH of the solution and the presence of specific scavengers. The optimal conditions for photocatalytic degradation were achieved at neutral pH, with $^{\bullet}$OH radicals identified as the key reactive species, while the other species, though less significant, also contribute to the overall degradation process.

4.3 Intermediates in the MG dye photocatalytic pathway

To illuminate the degradation mechanisms of MG dye, high-resolution mass spectrometry (HRMS) was employed to analyse the intermediate products formed during the photocatalytic process, as illustrated in Fig. 11. The initial mass spectrum of MG dye reveals a prominent peak at m/z 329, corresponding to the molecular mass of the MG cationic dye, which lacks chlorine. Remarkably, within just 5 minutes of adding the Co@BFO-III catalyst, the peak at m/z 329 diminished significantly, indicating the rapid degradation of the MG dye. Concurrently, several new peaks emerged, signifying the formation of degradation intermediates and by-products. The analysis delineated two distinct degradation pathways based on the observed intermediates.

Pathway (a) involves the N-demethylation of MG, producing intermediates 1a (m/z 315), 1b (m/z 301), and 1c (m/z 273). The degradation process continues as intermediate 1c undergoes further reactions, including deamination and oxidative cleavage of the chromophore, yielding 1d (m/z 195). This pathway ultimately leads to the formation of mineralized products, indicating complete degradation of the dye.

Pathway (b) is characterized by the radical-mediated oxidative cleavage of the MG chromophore, resulting in the formation of
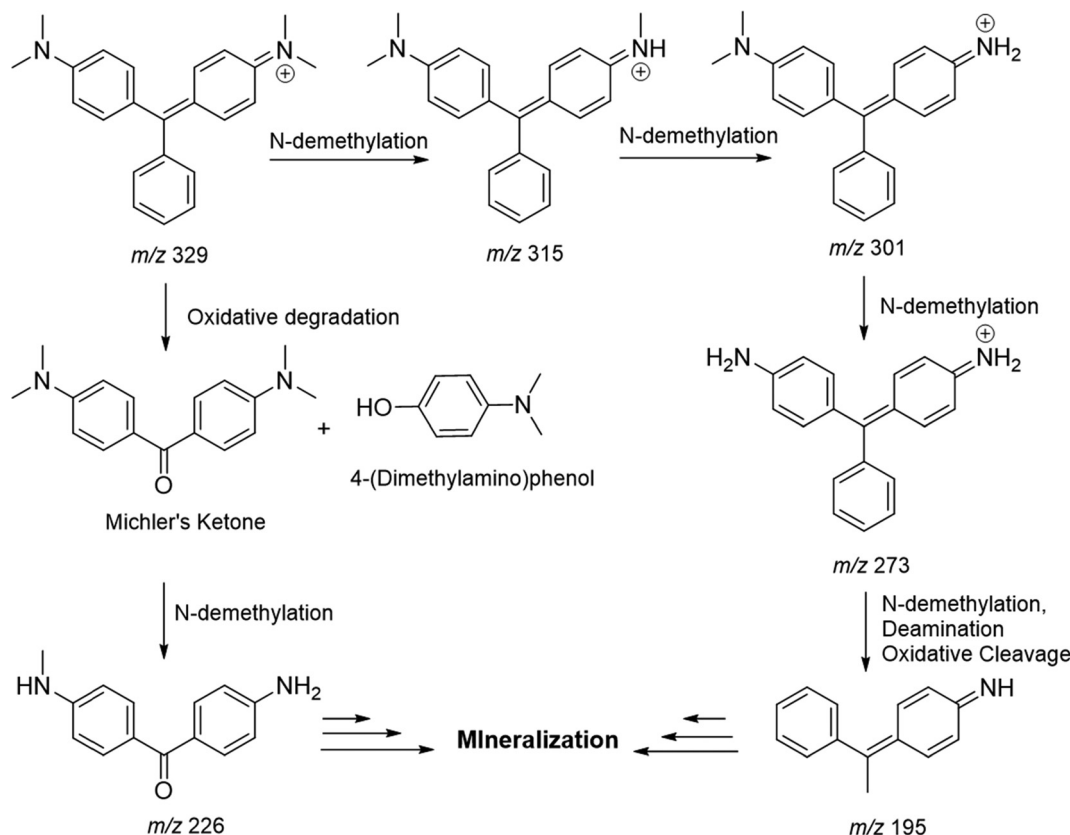
Fig. 11 Intermediate generation during MG dye photocatalysis over a Co@BFO-III nanocomposite.

Michler's ketone (2a) and 4-(dimethylamino)phenol (3a, m/z 137). Subsequent N-demethylation of Michler's ketone (2a) generates intermediate 2b (m/z 226). Following a series of oxidative degradation steps, this pathway also leads to the production of mineralized products.

4.4 Antibacterial properties

The antibacterial properties of the Co@BFO-III nanocomposite were evaluated against the Gram-negative bacterium *Klebsiella pneumoniae* and the Gram-positive bacterium *Bacillus cereus* using the agar well diffusion assay, as depicted in Fig. 12. The results indicate that the Co@BFO-III nanocomposite exhibits

Fig. 12 Antimicrobial properties of the fabricated Co@BFO-III. (a) *Bacillus cereus*, (b) *Klebsiella pneumonia*; (1) ddH$_2$O; (2) gentamicin; (3) streptomycin; (4) Co@BFO-III.

significant growth inhibitory effects on both bacterial strains. Notably, the zone of inhibition was larger for *K. pneumoniae* compared to *B. cereus*, suggesting a higher susceptibility of the Gram-negative bacteria to the Co@BFO-III nanocomposite. This observation aligns with previous studies indicating that Gram-negative bacterial strains often demonstrate increased sensitivity to such photocatalytic materials.[55,56] The minimal inhibitory concentration (MIC) of the Co@BFO-III nanocomposite against the selected bacterial strains was determined by monitoring the growth rate in culture media supplemented with various concentrations (0 to 15 μg ml^{-1}) of the nanocomposite. The results revealed a dose-dependent response, with significant suppression of growth observed within the first 2 hours of exposure at concentrations between 10 to 15 μg ml^{-1}. The MIC value for both *K. pneumoniae* and *B. cereus* was found to be 10 μg ml^{-1}, indicating that Co@BFO-III is an effective bactericidal agent at this concentration.

The antibacterial activity of the Co@BFO-III nanocomposite can be attributed to several mechanisms. The unique structural properties of the nanocomposite enhance its interaction with bacterial cell membranes, leading to increased permeability and eventual cell lysis. The generation of reactive oxygen species (ROS) upon exposure to light significantly contributes to oxidative stress within bacterial cells, which damages critical cellular components such as proteins and DNA. Moreover, the release of Co^{2+} ions from the Co@BFO-III nanocomposite may interfere with essential ion uptake, further exacerbating cellular dysfunction. The ability of
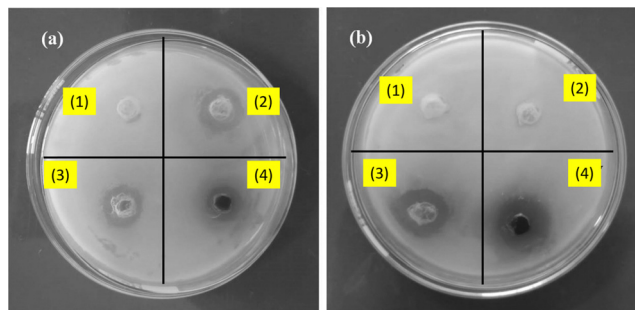
Co@BFO-III to generate ROS and disrupt cellular integrity positions it as a promising candidate for controlling infections caused by foodborne bacterial strains. In conclusion, the Co@BFO-III nanocomposite demonstrates significant antimicrobial properties against both *K. pneumoniae* and *B. cereus*, making it a viable option for applications in antimicrobial treatments and environmental remediation strategies.

4.5 Anti-oxidant activity

The antioxidant activity of the biogenic Co@BFO-III nanocomposite was assessed through 2,2-diphenyl-1-picrylhydrazyl (DPPH) radical scavenging and total antioxidant capacity (TAC) assays. The results indicate a significant concentration-dependent inhibitory effect on DPPH radicals across all tested concentrations of the Co@BFO-III nanocomposite, ranging from 2.5 mg L^{-1} to 15 mg L^{-1}. Specifically, the DPPH radical scavenging activity exhibited an increase from 14.8% to 84.8% as the concentration of Co@BFO-III increased, demonstrating its strong potential as an antioxidant agent. The calculated IC$_{50}$ value for the DPPH scavenging activity of the Co@BFO-III nanocomposite was found to be 11.13 mg L^{-1}. This indicates that the nanocomposite is effective at relatively low concentrations, emphasizing its potential for applications in antioxidant therapy and as a dietary supplement.

Additionally, the TAC assay further corroborated the strong antioxidant properties of the synthesized Co@BFO-III nanocomposite, with an IC$_{50}$ value of 11 mg L^{-1} observed across all tested concentrations. This consistent performance underscores the reliability of the nanocomposite as a free radical scavenger.

Moreover, the electrostatic interactions between the functional groups present on the surface of Co@BFO-III (such as COO^{-} and OH) and the radical species likely enhance its scavenging efficacy. These interactions facilitate the binding of reactive oxygen species (ROS) to the nanocomposite, promoting the conversion of harmful radicals into less reactive species, thus reducing oxidative stress. The presence of these functional biomolecules not only contributes to the antioxidant activity of the Co@BFO-III nanocomposite but also plays a synergistic role in enhancing its overall bioactivity. The structural integrity and surface characteristics of the nanocomposite are critical in maximizing these interactions, ultimately leading to superior antioxidant performance.

In order to better understand the Co@BFO-III nanocomposite's photocatalytic efficiency the chemical oxygen demand (COD) of dye solutions was measured prior to as well as after light was introduced when a photocatalyst was present. The COD of the dye solution dropped from 269 to 78 mg L^{-1}. The mineralization yield of the nanocomposite after being exposed to radiation was determined to be 71%.

In summary, the Co@BFO-III nanocomposite exhibits strong antioxidant activity, as demonstrated by its effective DPPH scavenging and total antioxidant capacity. The results highlight the potential of this nanocomposite for use in applications aimed at reducing oxidative stress and promoting health benefits through its natural antioxidant properties.

The photocatalytic performance of the Co@BFO-III nanocomposite was evaluated for its recyclability and stability, confirming its suitability for practical applications. The Co@BFO-III nanocomposite, recognized for its superior photocatalytic efficiency, was subjected to four consecutive cycles of solar light irradiation under identical experimental conditions. After each cycle, the catalyst was recovered through centrifugation for reuse in subsequent experiments. The results of the photocatalytic degradation efficiency are illustrated in the reusability graph (Fig. 13(a)). The initial run exhibited a degradation efficiency of 97%, while the subsequent runs showed slightly reduced efficiencies of 93%, 89%, and 85%, respectively. This minor decline in performance indicates that the Co@BFO-III nanocomposite retains a high level of photocatalytic activity even after multiple uses. The initial high efficiency can be attributed to the availability of active sites on the catalyst surface. The observed decrease in efficiency during the later runs is likely due to a combination of factors, including the gradual diffusion of the catalyst during the recovery process and potential blocking of active sites by the dye and its
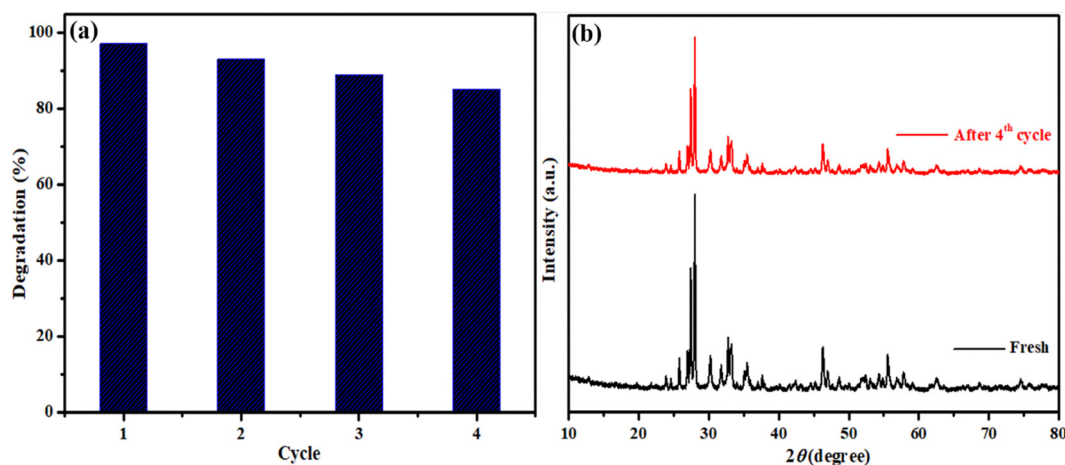

Fig. 13 (a) Reusability for MG dye photodegradation under sunlight, and (b) XRD patterns of fresh and reused Co@BFO nanocomposites.

Table 1 Comparison of the photodegradation proficiency for MG dye

Material	Dosage (mg)	Dye concentration (mg L^{-1})	Light sources	Time (min)	Degradation (%)	Ref.
CuO/PbO	20	2	Sunlight	40	100	57
CH/Ce/ZnO	50	5	Visible light	90	87	58
N–Na–Fe–TiO$_2$	110	100	UV light	30	96.6	59
Fe^{3+}/TiO$_2$	NA	5	UV light	110	85	60
ZnO/CNT	10	30	UV light	60	79	61
Fe$_2$O$_3$/SnO$_2$	40	100	Sunlight	240	86	62
La-BDC MOFs	50	60	UV light	60	98	63
Co@BFO	40	15	Sunlight	120	97	This study

degradation by-products. To further assess the stability of the Co@BFO-III nanocomposite, the XRD patterns of the photo-catalyst were analyzed before and after the four cycles of photocatalytic testing (Fig. 13(b)). The XRD analysis revealed no significant changes in the crystallinity of the recycled sample, suggesting that the structural integrity of the photocatalyst is well maintained even after repeated use. This finding highlights the excellent stability of the Co@BFO-III nanocomposite under pro-longed solar irradiation and experimental conditions.

In summary, the Co@BFO-III nanocomposite demonstrates remarkable recyclability and stability, maintaining high photo-catalytic efficiency across multiple cycles. Its resilience to structural changes and retention of active sites makes it a promising candidate for sustainable applications in environ-mental remediation.

To evaluate the superior performance of the as-prepared Co@BFO nanocomposite photocatalyst in this study, a com-parative analysis was conducted with previously reported photocatalysts documented in the literature for the degradation of malachite green (MG) dye. The comparison, summarized in Table 1, highlights various photocatalysts, their dosages, dye concentrations, light sources, exposure times, and corres-ponding degradation efficiencies. Among the reviewed materi-als, the Co@BFO nanocomposite demonstrated an impressive degradation efficiency of 97% at a dosage of 40 mg and a dye concentration of 15 mg L^{-1} under sunlight irradiation for 120 minutes. This performance is notably superior when com-pared to other photocatalysts, such as CuO/PbO, which achieved complete degradation (100%) in a shorter time (40 min) with a lower dye concentration (2 mg L^{-1}). However, the efficacy of the Co@BFO nanocomposite at a higher dye concentration reflects its robustness and effectiveness in real-world applications. In contrast, several other photocatalysts, such as CH/Ce/ZnO and N–Na–Fe–TiO$_2$, displayed varying degrees of effectiveness, achieving 87% and 96.6% degradation efficiencies, respectively. These comparisons indicate that while some photocatalysts can achieve higher degradation rates under specific conditions, the Co@BFO nanocomposite's per-formance at a moderate concentration and extended exposure time demonstrates its practical applicability for treating more concentrated dye solutions. Furthermore, photocatalysts like ZnO/CNT and Fe$_2$O$_3$/SnO$_2$ showed lower degradation efficien-cies of 79% and 86%, respectively, even under UV and sunlight exposure, indicating that the Co@BFO nanocomposite has a competitive advantage in terms of efficiency and versatility. The

La-BDC MOFs also exhibited a high degradation rate of 98%, but the conditions of that study (50 mg dosage, 60 mg L^{-1} concentration) differed significantly from those used in this research. In conclusion, the Co@BFO nanocomposite emerges as a highly efficient photocatalyst for the degradation of MG dye, outperforming many traditional photocatalysts under comparable conditions. This enhanced photocatalytic activity can be attributed to its unique structural properties and the synergistic effects of cobalt doping, which facilitate efficient charge separation and the generation of reactive species.

5. Conclusion

In summary, this study successfully demonstrates the synthesis and multifunctional applications of the Co-doped BiFeO$_3$ nano-composite (Co@BFO-III), highlighting its exceptional photoca-talytic, antibacterial, and antioxidant properties. The Co@BFO-III nanocomposite achieved a remarkable 97% degradation of malachite green dye under sunlight irradiation, showcasing its efficiency as a photocatalyst in addressing environmental pol-lutants. The study also reveals the material's potent antibacter-ial activity against both *Klebsiella pneumoniae* and *Bacillus cereus*, with a minimal inhibitory concentration (MIC) of 10 μg mL^{-1}, indicating its potential as an effective antimicro-bial agent for foodborne infections. Additionally, the Co@BFO-III nanocomposite exhibited substantial antioxidant activity, with a DPPH radical scavenging efficiency showing a clear concentration-dependent response. These findings underscore the nanocomposite's versatility and effectiveness, positioning it as a promising candidate for diverse applications in environ-mental remediation and public health. The successful demon-stration of multifunctionality in a single nanocomposite opens new avenues for future research, particularly in optimizing synthesis techniques and exploring additional applications in catalysis and biomedicine. The insights gained from this work not only contribute to the existing body of knowledge in nanotechnology but also hold promise for practical implemen-tations in real-world scenarios, ultimately advancing the field of sustainable materials and environmental management.

Author contributions

Conceptualization: Sandeep Kaushal, Rahul Badru; methodo-logy: Sandeep Kaushal, Satya Vir Sharma, Sanjeev Kumar and

Jasvir Dalal; validation: Sandeep Kaushal, Yadwinder Singh, Gautam Singh and Sandeep Kumar; formal analysis: Sandeep Kaushal, Sandeep Kumar and Supreet; writing – original draft: Sandeep Kaushal, Sandeep Kumar, and Rahul Badru; writing – review and editing: Sandeep Kaushal, and Sanjeev Kumar; supervision: Sandeep Kaushal and Satya Vir Sharma. All the authors have read and agreed to the published version of the manuscript.

Data availability

The data that support the findings of this study are available from the Royal Society of Chemistry, but restrictions apply to the availability of these data, which were used under license for the current study, and so are not publicly available. Data are however available from the authors upon reasonable request and with permission of the Royal Society of Chemistry.

Conflicts of interest

There are no conflicts to declare.

References

1 F. Chen, Q. Yang, X. Li, G. Zeng, D. Wang, C. Niu, J. Zhao, H. An, T. Xie and Y. Deng, Hierarchical assembly of graphene-bridged $Ag_3PO_4/Ag/BiVO_4$ (040) Z-scheme photocatalyst: An efficient, sustainable and heterogeneous catalyst with enhanced visible-light photoactivity towards tetracycline degradation under visible light irradiation, *Appl. Catal., B*, 2017, **200**, 330–342, DOI: **10.1016/j.apcatb.2016.07.021**.

2 S. Kaushal, V. Kumari and P. P. Singh, Sunlight-driven photocatalytic degradation of ciprofloxacin and organic dyes by biosynthesized $rGO–ZrO_2$ nanocomposites, *Environ. Sci. Pollut. Res.*, 2023, **30**, 65602–65617, DOI: **10.1007/s11356-023-27000-6**.

3 H. Kaur, S. Kumar, S. Kaushal, R. Badru, P. P. Singh and A. Pugazhendhi, Highly customized porous TiO_2-PANI nanoparticles with excellent photocatalytic efficiency for dye degradation, *Environ. Res.*, 2023, **225**, 114960, DOI: **10.1016/j.envres.2022.114960**.

4 Z. H. Jaffari, S. M. Lam, J. C. Sin and A. R. Mohamad, Constructing magnetic Pt-loaded $BiFeO_3$ nanocomposite for boosted visible light photocatalytic and antibacterial activities, *Environ. Sci. Pollut. Res.*, 2019, **26**, 10204–10218, DOI: **10.1007/s11356-019-04503-9**.

5 S. Iqbal, F. Bibi, M. F. Elasadek and M. Jamshaid, Gd and Ni co-doped $BiFeO_3$ ferrite/r-GO nanocomposite for photocatalytic environmental remediation applications, *Mater. Sci. Semicond. Process.*, 2024, **179**, 108529, DOI: **10.1016/j.mssp.2024.108529**.

6 M. T. Kebede, V. Dillu, S. Devi and S. Chauhan, A comparative investigation of structural, magnetic and photocatalytic properties of pure, Ce–Ni and Cd–Ni co-doped $BiFeO_3$ nanoparticles, *Mater. Sci. Eng. B*, 2024, **301**, 117188, DOI: **10.1016/j.mseb.2024.117188**.

7 Z. Chen, Y. Liu, W. Wei and B. J. Ni, Recent advances in electrocatalysts for halogenated organic pollutant degradation, *Environ. Sci.: Nano*, 2019, **6**, 2332–2366, DOI: **10.1039/C9EN00411D**.

8 T. Pan, H. Liu, M. Jiang, J. Li, W. Liu, Q. Jiao and T. Zhang, New insights into the adsorption behavior of thiacloprid at the microfibers/water interface: Role of humic acid, *Chemosphere*, 2023, **311**, 136938, DOI: **10.1016/j.chemosphere.2022.136938**.

9 S. Kaushal, P. P. Singh and N. Kaur, Metal organic framework-derived Zr/Cu bimetallic photocatalyst for the degradation of tetracycline and organic dyes, *Environ. Nanotechnol., Monit. Manage.*, 2022, **18**, 100727, DOI: **10.1016/j.enmm.2022.100727**.

10 K. Bano, S. Kaushal, B. Lal, S. K. Joshi, R. Kumar and P. P. Singh, Fabrication of CuO/ZnO heterojunction photocatalyst for efficient photocatalytic degradation of tetracycline and ciprofloxacin under direct sun light, *Environ. Nanotechnol., Monit. Manage.*, 2023, **20**, 100863, DOI: **10.1016/j.enmm.2023.100863**.

11 M. Saeed, M. Muneer, A. Haq and N. Akram, Photocatalysis: An effective tool for photodegradation of dyes—A review, *Environ. Sci. Pollut. Res.*, 2022, **29**, 293–311, DOI: **10.1007/s11356-021-16389-7**.

12 Z. Cai, Z. Sun, W. Liu, F. Pan, P. Sun and J. Fu, An overview of nanomaterials applied for removing dyes from wastewater, *Environ. Sci. Pollut. Res.*, 2017, **24**, 15882–15904, DOI: **10.1007/s11356-017-9003-8**.

13 L. Zhang, S. Hou, T. Wang, S. Liu, X. Gao, C. Wang and G. Wang, Recent Advances in Application of Graphitic Carbon Nitride-Based Catalysts for Photocatalytic Nitrogen Fixation, *Small*, 2022, **18**(28), e2202252, DOI: **10.1002/smll.202202252**.

14 Y. Yuan, R. Guo, L. Hong, X. Ji, Z. Lin, Z. Li and W. Pan, A review of metal oxide-based Z-scheme heterojunction photocatalysts: actualities and developments, *Mater. Today Energy*, 2021, **21**, 100829, DOI: **10.1016/j.mtener.2021.100829**.

15 K. Kaur, R. Badru, P. P. Singh and S. Kaushal, Photodegradation of organic pollutants using heterojunctions: A review, *J. Environ. Chem. Eng.*, 2020, **8**, 103666, DOI: **10.1016/j.jece.2020.103666**.

16 R. Boppella, W. Yang, J. Tan, H. C. Kwon, J. Park and J. Moon, Black phosphorus supported Ni_2P co-catalyst on graphitic carbon nitride enabling simultaneous boosting charge separation and surface reaction, *Appl. Catal., B*, 2019, **242**, 422–430, DOI: **10.1016/j.apcatb.2018.10.018**.

17 J. Kong, Z. Rui, X. Wang, H. Ji and Y. Tong, Visible-light decomposition of gaseous toluene over $BiFeO_3–(Bi/Fe)_2O_3$ heterojunctions with enhanced performance, *J. Chem. Eng.*, 2016, **302**, 552–559, DOI: **10.1016/j.cej.2016.05.100**.

18 X. Xu, X. Ding, X. Yang, P. Wang, S. Li, Z. Lu and H. Chen, Oxygen vacancy boosted photocatalytic decomposition of ciprofloxacin over Bi_2MoO_6: Oxygen vacancy engineering,

biotoxicity evaluation and mechanism study, *J. Hazard. Mater.*, 2019, **364**, 691–699, DOI: 10.1016/j.jhazmat.2018.10.063.

19 S. Salimi, R. Sotudeh-Gharebagh, R. Zarghami, S. Y. Chan and K. H. Yuen, Production of naocellulose and its applications in drug delivery: A critical review, *ACS Sustainable Chem. Eng.*, 2019, 7(19), 15800–15827, DOI: 10.1021/acssuschemeng.9b02744.

20 H. Maleki, Characterization and photocatalytic activity of Y-doped BiFeO$_3$ ceramics prepared by solid-state reaction method, *Adv. Powder Technol.*, 2019, **30**, 2832–2840, DOI: 10.1016/j.apt.2019.08.031.

21 C. C. Zhang, J. Q. Dai and X. L. Liang, Enhanced ferroelectric properties of (Zn, Ti) equivalent co-doped BiFeO$_3$ films prepared via the sol-gel method, *Ceram. Int.*, 2021, **47**, 16776–16785, DOI: 10.1016/j.ceramint.2021.02.250.

22 T. Liu, Y. Xu and J. Zhao, Low-Temperature Synthesis of BiFeO$_3$ *via* PVA Sol–Gel Route, *J. Am. Ceram. Soc.*, 2010, **93**, 3637–3641, DOI: 10.1111/j.1551-2916.2010.03945.x.

23 M. S. Akhtar, Y. G. Alghamdi, M. A. Malik, R. M. A. Khalil, S. Riaz and S. Naseem, Structural, optical, magnetic and half-metallic studies of cobalt doped ZnS thin films deposited *via* chemical bath deposition, *J. Mater. Chem. C*, 2015, **3**, 6755–6763, DOI: 10.1039/C5TC00557D.

24 H. Fki, M. Koubaa, L. Sicard, W. Cheikhrouhou-Koubaa, A. Cheikhrouhou and S. Ammar-Merah, Influence of Y doping on structural, vibrational, optical and magnetic properties of BiFeO$_3$ ceramics prepared by Mechanical Activation, *Ceram. Int.*, 2017, **43**, 4139–4150, DOI: 10.1016/j.ceramint.2016.12.028.

25 M. Othman, I. Mallek-Zouari, H. Akrout and N. T. Mliki, Synthesis and properties of ultra-small BiFeO$_3$ nanoparticles doped with cobalt, *Ceram. Int.*, 2023, **49**, 10580–10587, DOI: 10.1016/j.ceramint.2022.11.245.

26 G. R. Rodrigues, C. Abarrategui, I. S. Gómez, S. C. Dias, A. O. González and O. L. Franco, Antimicrobial magnetic nanoparticles based-therapies for controlling infectious diseases, *Int. J. Pharm.*, 2019, **30**(555), 356–367, DOI: 10.1016/j.ijpharm.2018.11.043.

27 A. Mobed, M. Hasanzadeh and F. Seidi, Anti-bacterial activity of gold nanocomposites as a new nanomaterial weapon to combat photogenic agents: recent advances and challenges, *RSC Adv.*, 2021, **11**, 34688–34698, DOI: 10.1039/D1RA06030A.

28 L. Viganor, O. Howe, P. McCarron, M. Mccann and M. Devereux, The Antibacterial Activity of Metal Complexes Containing 1,10-phenanthroline: Potential as Alternative Therapeutics in the Era of Antibiotic Resistance, *Curr. Top. Med. Chem.*, 2017, **17**(11), 1280–1302, DOI: 10.2174/1568026616666161003143333.

29 A. Mobed, M. Hasanzadeh and F. Seidi, Anti-bacterial activity of gold nanocomposites as a new nanomaterial weapon to combat photogenic agents: recent advances and challenges, *RSC Adv.*, 2021, **11**, 34688–34698, DOI: 10.1039/D1RA06030A.

30 K. Kumar, R. Kumar, R. Jasrotia, S. Kalia, V. Arya, A. Kumar, R. Khargotra and N. Thakur, *Discover Appl. Sci.*, 2024, **6**, 1–19, DOI: 10.1007/s42452-024-05679-7.

31 S. Balaji and M. B. Kumar, Facile green synthesis of zinc oxide nanoparticles by *Eucalyptus globulus* and their photocatalytic and antioxidant activity, *Adv. Powder Technol.*, 2017, **28**, 785–797, DOI: 10.1016/j.apt.2016.11.026.

32 H. Sadiq, A. Sohail, A. Basit, N. Akhtar, K. Batool, S. Hisaindee and L. Asghar, Assessment of antioxidant activity of pure graphene oxide (GO) and composite V$_2$O$_5$/GO using DPPH radical and H$_2$O$_2$ scavenging assays, *J. Sol-Gel Sci. Technol.*, 2023, **108**, 840–849, DOI: 10.1007/s10971-023-06231-6.

33 Z. Shan, F. Ma, S. You, L. Shan, D. Kong, H. Guo and C. Cui, Enhanced visible light photo-Fenton catalysis by lanthanum-doping BiFeO$_3$ for norfloxacin degradation, *Environ. Res.*, 2023, **216**, 114588, DOI: 10.1016/j.envres.2022.114588.

34 Udayabhanu, P. C. Nethravathi, M. A. P. Kumar, D. Suresh, K. Lingaraju, H. Rajanaika, H. Nagabhushana and S. C. Sharma, *Tinospora cordifolia* mediated facile green synthesis of cupric oxide nanoparticles and their photocatalytic, antioxidant and antibacterial properties, *Mater. Sci. Semicond. Process.*, 2015, **33**, 81–88, DOI: 10.1016/j.mssp.2015.01.034.

35 Y. Singh, S. Kaushal and R. S. Sodhi, Biogenic synthesis of silver nanoparticles using cyanobacterium *Leptolyngbya* sp. WUC 59 cell-free extract and their effects on bacterial growth and seed germination, *Nanoscale Adv.*, 2020, **2**, 3972–3982, DOI: 10.1039/D0NA00357C.

36 P. Peddi, P. R. Ptsrk, N. U. Rani and S. L. Tulasi, Green synthesis, characterization, antioxidant, antibacterial, and photocatalytic activity of *Suaeda maritima* (L.) Dumort aqueous extract-mediated copper oxide nanoparticles, *J. Genet. Eng. Biotechnol.*, 2021, **19**, 131, DOI: 10.1186/s43141-021-00229-9.

37 S. Srihasam, K. Thyagarajan, M. Korivi, V. R. Lebaka and S. P. Mallem, Phytogenic generation of NiO nanoparticles using Stevia leaf extract and evaluation of their in-vitro antioxidant and antimicrobial properties, *Biomolecules*, 2020, **10**, 89, DOI: 10.3390/biom10010089.

38 M. Sun, L. Bai, W. Ma, Y. Liu, J. Zhang and J. Yang, Ho and Ti Co-substitution tailored structural phase transition and enhanced magnetic properties of BiEeO$_3$ thin films, *ACS Omega*, 2020, **5**, 29292–29299, DOI: 10.1021/acsomega.0c04076.

39 T. Soltani and B. K. Lee, Novel and facile synthesis of Ba-doped BiFeO$_3$ nanoparticles and enhancement of their magnetic and photocatalytic activities for complete degradation of benzene in aqueous solution, *J. Hazard. Mater.*, 2016, **316**, 122–133, DOI: 10.1016/j.jhazmat.2016.03.052.

40 T. Gao, Z. Chen, Y. Zhu, F. Niu, Q. Huang, L. Qin, X. Sun and Y. Huang, Synthesis of BiFeo$_3$ nanoparticles for the visible-light induced photocatalytic property, *Mater. Res. Bull.*, 2014, **59**, 6–12, DOI: 10.1016/j.materresbull.2014.06.022.

41 H. Lv, X. Shen, Z. Ji, D. Qiu, G. Zhu and Y. Bi, Synthesis of graphene oxide-BiPO$_4$ composites with enhanced photocatalytic properties, *Appl. Surf. Sci.*, 2013, **284**, 308–314, DOI: 10.1016/j.apsusc.2013.07.098.

42 M. Abushad, W. Khan, S. Naseem, S. Hussain, M. Nadeem and A. Ansari, Influence of Mn doping on microstructure,

optical, dielectric and magnetic properties of $BiFeO_3$ nano-ceramics synthesized *via* sol–gel method, *Ceram. Int.*, 2019, **45**, 7437–7445, DOI: **10.1016/j.ceramint.2019.01.035**.

43 N. Zhang, D. Chen, F. Niu, S. Wang, L. Qin and Y. Huang, Enhanced visible light photocatalytic activity of Gd doped $BiFeO_3$ nanoparticles and mechanism insight, *Sci. Rep.*, 2016, **20**, 26467, DOI: **10.1038/srep26467**.

44 J. Yang, M. K. Choi, D. H. Kim and T. Hyeon, Designed Assembly and Integration of Colloidal Nanocrystals for Device Applications, *Adv. Mater.*, 2014, **26**, 1207–1216, DOI: **10.1002/adma.201502851**.

45 C. Cummins, D. Borah, S. Rasappa, A. Chaudhari, T. Ghoshal, B. Driscoll and M. A. Morris, Self-assembly of polystyrene-*block*-poly(4-vinylpyridine) block copolymer on molecularly functionalized silicon substrates: fabrication of inorganic nanostructured etchmask for lithographic use, *J. Mater. Chem. C*, 2013, **1**, 7941–7951, DOI: **10.1039/C3TC31498G**.

46 S. Kalasina, K. Kongsawatvoragul, N. Phattharasupakun, P. Phattharaphuti and M. Sawangphruk, *RSC Adv.*, 2020, **10**, 14154–14160, DOI: **10.1039/d0ra01714k**.

47 J. Jiang, J. Zou, M. N. Anjum, J. Yan, L. Huang, Y. Zhang and J. Chen, Synthesis and characterization of wafer-like $BiFeO_3$ with efficient catalytic activity, *Solid State Sci.*, 2011, **13**, 1779–1785, DOI: **10.1016/j.solidstatesciences.2011.07.008**.

48 K. M. Reza, A. S. W. Kurny and F. Gulshan, Parameters affecting the photocatalytic degradation of dyes using TiO_2: a review, *Appl. Water Sci.*, 2017, **7**, 1569–1578, DOI: **10.1007/s13201-015-0367-y**.

49 E. M. Saggioro, A. S. Oliveira, T. Pavesi, C. G. Maia, L. F. V. Ferreira and J. C. Moreira, Use of titanium dioxide photocatalysis on the remediation of model textile waste-waters containing azo dyes, *Molecules*, 2011, **16**(12), 10370–10386, DOI: **10.3390/molecules161210370**.

50 T. Chen, C. Cao, T. Chen, X. Ding, H. Huang, L. Shen, X. Cao, M. Zhu, J. Xu, J. Gao and Y. F. Han, Unraveling Highly Tunable Selectivity in CO_2 Hydrogenation over Bimetallic In-Zr Oxide Catalysts, *ACS Catal.*, 2019, **9**, 8785–8797, DOI: **10.1021/acscatal.9b01869**.

51 T. Ali, A. Ahmed, U. Alam, I. Uddin, P. Tripathi and M. Muneer, Enhanced photocatalytic and antibacterial activities of Ag-doped TiO_2 nanoparticles under visible light, *Mater. Chem. Phys.*, 2018, **212**, 325–335, DOI: **10.1016/j.matchemphys.2018.03.052**.

52 J. Yang, R. Pang, D. Song and M. B. Li, Tailoring silver nanoclusters *via* doping: advances and opportunities, *Nanoscale Adv.*, 2021, **3**, 2411–2422, DOI: **10.1039/D1NA00077B**.

53 R. J. Tayade, T. S. Natarajan and H. C. Bajaj, Photocatalytic degradation of methylene blue dye using ultraviolet light emitting diodes, *Ind. Eng. Chem. Res.*, 2009, **48**, 10262–10267, DOI: **10.1021/ie9012437**.

54 S. Kaushal, P. Kurichh and P. Singh, Novel 3D flower like ZnO/MnV_2O_6 heterojunction as an efficient adsorbent for the removal of imidacloprid and photocatalyst for degradation of organic dyes in waste water, *Polyhedron*, 2021, **201**, 115161, DOI: **10.1016/j.poly.2021.115161**.

55 P. Yugandhar, T. Vasavi, P. U. M. Devi and N. Savithramma, Bioinspired green synthesis of copper oxide nanoparticles from Syzygium alternifolium (Wt.) Walp: characterization and evaluation of its synergistic antimicrobial and anticancer activity, *Appl. Nanosci.*, 2017, **7**, 417–427, DOI: **10.1007/s13204-017-0584-9**.

56 D. Singh, D. Jain, D. Rajpurohit, G. Jat, H. S. Kushwaha, A. Singh, S. R. Mohanty, M. K. Al-Sadoon, W. Zaman and S. K. Upadhyay, Bacteria assisted green synthesis of copper oxide nanoparticles and their potential applications as antimicrobial agents and plant growth stimulants, *Front. Chem.*, 2023, **11**, 1154128, DOI: **10.3389/fchem.2023.1154128**.

57 P. M. Bradley, K. M. Romanok, K. L. Smalling, J. R. Masoner, D. W. Kolpin and S. E. Gordon, Predicted aquatic exposure effects from a national urban stormwater study, *Environ. Sci.: Water Res. Technol.*, 2023, **9**, 3191–3199, DOI: **10.1039/D2EW00933A**.

58 A. M. Saad, M. R. Abukhadra, S. A. K. Ahmed, A. M. Elzanaty, A. H. Mady, M. A. Betiha, J. J. Shim and A. M. Rabie, Photocatalytic degradation of malachite green dye using chitosan supported ZnO and Ce–ZnO nano-flowers under visible light, *Environ. Manage.*, 2020, **258**, 110043, DOI: **10.1016/j.jenvman.2019.110043**.

59 S. Zhang, Q. Lu, C. Zhang, Y. Zhou, M. Liu, Y. Zhang and L. Deng, Green synthesis of silver–carbon nanocomposites with extraordinary stability and robust antibacterial activity against bacterial diseases in fish, *ACS Appl. Bio Mater.*, 2022, **5**(3), 1064–1072, DOI: **10.1021/acsabm.1c01116**.

60 M. Asiltürk, F. Sayılkan and E. Arpaç, Effect of Fe^{3+} ion doping to TiO_2 on the photocatalytic degradation of Malachite Green dye under UV and Vis-irradiation, *J. Photochem. Photobiol., A*, 2009, **203**, 64–71, DOI: **10.1016/j.jphotochem.2008.12.021**.

61 N. Arsalani, S. Bazazi, M. Abuali and S. Jodeyri, A new method for preparing ZnO/CNT nanocomposites with enhanced photocatalytic degradation of malachite green under visible light, *J. Photochem. Photobiol., A*, 2020, **389**, 112207, DOI: **10.1016/j.jphotochem.2019.112207**.

62 G. K. Pradhan, K. H. Reddy and K. M. Parida, Facile fabrication of mesoporous α-Fe_2O_3/SnO_2 nanoheterostructure for photocatalytic degradation of malachite green, *Catal. Today*, 2014, **224**, 171–179, DOI: **10.1016/j.cattod.2013.10.038**.

63 A. I. Saber, K. Sharma, S. Aggarwal, A. Babbar, R. Kumar, A. Kaur, R. Badru and S. Kaushal, Efficient photocatalytic degradation of tetracycline antibiotic and melachite green dye using La-BDC MOFs, *Emergent Mater.*, 2024, **7**, 1019–1030, DOI: **10.1007/s42247-024-00644-x**.